Building interface bonding and shield for stable Li-rich Mn-based oxide cathode

Jun Chen, [a] Hongyi Chen, [a] Yu Mei, [a] Jinqiang Gao, [a] Alvin Dai, [b] Ye Tian, [a] Wentao Deng, [a] Guoqiang Zou[a], Hongshuai Hou, [a] Craig E. Banks, [d] Tongchao Liu, [b] Khalil Amine, [b,c] Xioabo Ji[a]

[a]State Key Laboratory of Powder Metallurgy, College of Chemistry and Chemical Engineering, Central South University, Changsha, China

[b]Chemical Sciences and Engineering Division, Argonne National Laboratory, Lemont, IL, USA

[c]Material Science and Engineering, Stanford University, Stanford, CA, USA

[d]Division of Chemistry and Environmental Science, Manchester Metropolitan University, Manchester, M1 5GD, UK

Corresponding authors.

xji@csu.edu.cn; liut@anl.gov.

1. Introduction

Li-rich Mn-based oxide (LRM) cathodes have attracted intensive attention as they render remarkable capacities by invoking redox chemistry on both transition metal (TM) and lattice oxygen [1], [2], [3]. However, owing to the intrinsic instability of oxygen anion, LRM cathode usually suffers from irreversible lattice oxygen loss [4]. It is widely accepted that, lattice oxygen loss accompanies side reaction at the LRM electrode/electrolyte interface that trigger the microscopic/macroscopic structure evolutions, including the unidirectional phase transformation, the formation of thicker cathode electrolyte interface as well as structure/morphology fracture, ultimately leading to a fast capacity/voltage degradation [3,5]. Therefore, enabling sustainable lattice oxygen redox and strengthening the electrode/electrolyte interface would be the key to boost the capability of Li^+ storage for LRM cathode materials.

Admittedly, much effort has been devoted to mitigating the fast electrochemical degradation, including constructing coating layer on the surface, engineering dopants into structure framework, and developing nano/micro-heterostructures. In particular, surface protective coating, a widely industrialized technology, has been effective at suppressing the parasitic reactions between surface lattice oxygen and electrolyte [6], [7], [8], [9]. However, so far physical surface protection shows a negligible improvement in lattice oxygen reversibility, as demonstrated by the persistence of oxygen release and voltage fade when operating at high voltages. Once oxygen loss occurs on the surface, the energy barrier for TM migration will be greatly reduced, and irreversible phase transition will occur [4]. More importantly, the generation of surface oxygen vacancies will significantly accelerate the diffusion of bulk oxygen during extended cycling [10]. This phenomenon, together with the continuous irreversible phase transition, will activate lower-voltage redox chemistry, which has been considered as the governing cause of the capacity/voltage fading. Consequently, it is of particular importance to searching for a novel strategy that could simultaneously protect surface lattice oxygen from side reaction and enhance oxygen redox reversibility.

In this work, we designed a novel surface engineering LRM coupled with the band coherency and interface shielding effect, which dramatically improves the electrochemical performance of LRM cathode materials. Benefitting from an autocatalytic plating reaction, the LRM cathode materials are able to be fully encapsulated by amorphous CoxB. Interestingly, based on the unique physicochemical properties of CoxB [11], we found that band coherency is ingeniously excited by the interface bonding

between surface structure of LRM and amorphous CoxB coating layer, which would lower the energy of O 2p states associated with the strengthened orbital hybridization of O 2p-Mn 3d to elevate the formation energy of oxygen vacancy, thereby considerably mitigating the lattice oxygen loss. Simultaneously, interface shielding effect is invoked by the functionalized coating layer, which is beneficial for mitigating the side reaction along with subsequent TMs dissolution, and ultimately rendering a well-knit electrode/electrolyte interface. Expectedly, with the assistance of structure/interface coupling effect, the as-designed CB-LRM cathode renders excellent long cycling stability after 200 loops with only 0.1535% capacity fading and 3.35 mV voltage decline per cycle.

2. Result and discussion

2.1. Dissecting the band coherency effect induced by the coating layer via density functional theory calculation

Symmetry labels for LiTMO2 correspond to the conventional Oh point group of TMO6 coordination, while those for Li2MnO3 correspond to the C2v point group of OMn2Li4 coordination [9]. In terms of Li-rich Mn-based oxide cathode, when O is coordinated by two Mn and four Li such as in Li2MnO3 (Fig. 1c) [12,13], the point symmetry of the OMn2Li4 octahedron is C2v. According to the point symmetry, the molecular orbitals can be named as follows: four O 2p orbitals constitute σ-type bonding (a1 and b2) and antibonding (a1* and b2*) molecular orbitals with Mn nd(eg), (n + 1)s, and (n + 1)p, while two O 2p orbitals along an Li-O-Li axis and two Mn nd(t2g) form π-type less-bonding (b1) and less-antibonding (b1*) molecular orbitals (Fig. 1c-e). As previously reported [4], in Li2MnO3 cathode, the energy level of O 2p is higher that of the occupied Mn nd(t2g). Thus, the occupied molecular orbital of b1* is primarily consisted of O 2p, which is responsible for an additional lattice oxygen redox reaction (Fig. 1c-e). Importantly, before the lattice oxygen is oxidized, this π-type interaction between the occupied O 2p and Mn nd(t2g) is weak (almost nonbonding), and the O 2p orbital near the Fermi level appears to be “orphaned”. However, after the oxidation of this antibonding b1* molecular orbital occurs, the corresponding Mn-O bond would become more robust with the larger b1/b1* splitting (Fig. 1d, e), therefore stabilizing the oxidized oxygen anion. In short, in Li-rich Mn-based oxide cathode, the lattice oxygen redox could be modulated by designing the band features, based on the energetics in the crystal field theory. To demonstrate the feasibility of band coherency between bulk structure and coating layer for mitigating the lattice oxygen loss, density functional theory (DFT) calculations are firstly introduced. As shown in Fig. 1a, for the atomistic details, first-principles calculations are conducted on the (131) crystallographic plane of Li2MnO3 as well as on the interface between the Li2MnO3 (131) crystallographic plane and amorphous CoxB. It should be noticed that, as shown in Fig. 1b, at the interface between Li2MnO3 (131) crystallographic plane and amorphous CoxB, Co and B are preferentially bonded with the surface lattice O of Li2MnO3 (named as interface bonding effect), rather than with Li or Mn. The interfacial Co-O and B-O bonding are stronger than the lattice Mn-O bonding, as obviously indicated by the stronger electron cloud sharing for the former in the charge density plot (Fig. 1b). That is to say, the band coherency could be excited by the interface bonding effect to some extent, mainly resulted from the as-designed coating layer of amorphous CoxB. More importantly, the band coherency induced by the introduction of amorphous CoxB is beneficial for lowering the energy of O 2p states (Fig. 1c-e), which have less high-energy states close to Fermi level than that of LRM (Fig. 1c). Therefore, it is concluded that, a band coherency triggered by the interface bonding effect is effectively manipulated by the formation of the

bonding/antibonding b1/b1* molecular orbitals through a π-type O 2p-Mn 3d(t2g) interaction induced by the design of coating layer of amorphous CoxB, and the corresponding Mn-O bond should become more vigorous with larger b1/b1* splitting, thus enhancing the formation energy of oxygen vacancy and stabilizing the oxidized lattice oxygen (Fig. 1f). Therefore, it is expected that the band coherency induced by the design of functionalized coating layer of amorphous CoxB is beneficial to enhance the stability of crystal structure and drive the reversible lattice oxygen redox, bring about the improved Li+ storage capacities.

2.2. Demystifying the structure/morphology evolution triggered by the autocatalytic plating

By virtue of the insights from DFT calculations results above (Fig. 1). To adequately verify and take advantage of the mentioned physical properties for the functionalized coating layer. Pristine LRM, a typical polycrystalline microstructure with spherical secondary particles (Fig. 2b, c), is prepared by a conventional co-precipitation route, followed by calcination with lithium hydroxide [14]. As expected, by using the autocatalytic plating strategy (Fig. 2a) [15,16], the modified LRM (denoted as CB-LRM) with integrally encapsulated by amorphous CoxB is successfully designed (Fig. 2e, f and Fig. 4a, g), and the detailed method is displayed in Supporting Information. Accordingly, the atomic compositions of the as-prepared samples are listed based on the results of inductive coupled plasma emission spectrometer (ICP), as presented in Table S1 with normalized formula Li1.2Mn0.54Ni0.13Co0.13O2 for the pristine LRM. Note that the compositions of amorphous CoxB are close to Co2.3B Furthermore, their crystal structures are investigated by X-ray diffraction (XRD), as shown in Fig. 3a, b, all diffraction peaks are accurately labeled with a hexagonal α-NaFeO2 (space group: R-3 m), except for weaker superlattice diffraction characteristic peaks between 20° and 23°, which are attributed to the (020) and (110) diffraction peaks of monoclinic Li2MnO3 (space group: C2/m), mainly resulted from the unique Li/Mn local ordering in the TM layers [17]. Moreover, it is found that, no characteristic diffraction peaks of CoxB are observed in Fig. S1a, demonstrating that the as-obtained CoxB coating layers are presented as amorphous feature. It should be emphasized that the distinct splitting-diffraction peaks of (006)/(012) and (018)/(110) are obviously presented (Fig. S1c), thoroughly showing that both LRM and CB-LRM have a well ordered layered structure, that is to say, which is beneficial to improve the Li+ shuttling [18]. These results above are in good line with those of previous studies [12], and STEM with annular bright-field (ABF) as well as high angle annular dark-field (HAADF) images (Fig. 4d-f). Moreover, it is noteworthy that, in clear, the intensity of (003) diffraction peak for the pristine LRM is stronger than that of CB-LRM (Fig. S1b), which is perhaps ascribed that the exposure of the bulk materials is partly shielded by the coating layer of amorphous CoxB [14], unambiguously suggesting that the coating layer has been successfully adhered on the surface of LRM. Resultantly, the coating layer of amorphous CoxB, as confirmed above, may be good for mitigating the side reaction of electrode/electrolyte interface and stabilizing the lattice oxygen, thereby enhancing the reversibility of Li+ storage.

Multiscale characterizations are further employed to investigate the structure properties of CoxB surface coating. As shown in Fig. 2b-g, the coating layers of amorphous CoxB (∼ 20 nm) with hierarchical structure are confirmed by the high-resolution field emission scanning electron microscope (FE-SEM) (Fig. 2e, f) and STEM (Fig. 4a). The mapping images of electron energy loss spectroscopy (EELS) also reveal that the bulk structure of CB-LRM is integrally covered by amorphous CoxB (Fig. 4g, h), which may be beneficial for evoking the band coherency between the bulk structure and coating layer through the interface bonding effect as well as protecting the active materials [19,20], to some extent. To gain better understanding of the interface bonding effect, X-ray photoelectron spectroscopy (XPS) analysis is applied to further explore the surface state and interfacial interaction of the as-designed samples. As shown in Fig. 3d-f, the CB-LRM with completely covered by amorphous CoxB is also confirmed by the intrigued evolution of XPS spectra, as expected. Interestingly, the distinct B-O bonding is clearly observed for CB-LRM (Fig. 3d, f), regarded as interface bonding effect, which would be conducive to exciting the band coherency as well as stabilizing the lattice oxygen and reinforcing the stability of crystal structure through the interface bonding effect. These intriguing phenomena are in good line with DFT results (Fig. 1). Based on the results above, it is proposed that, the structure/interface coupling effect would be evoked by the coating layer of amorphous CoxB, which would be levers to strengthen the lattice oxygen and protect the active materials, therefore improving the capability of Li+ storage.

The fine structures of CB-LRM at the atomic scale are systematically probed by ABF/HAADF-STEM. As shown in Fig. 4d, e, the positions of TMs atoms are presented by bright-dot in HAADF-STEM images and dark-dot in ABF-STEM images. Both ABF and HAADF images confirm a typical composite structure composing of R-3 m and C2/m space group, which is well consistent with the XRD results [9, 21]. Moreover, the amorphous structure of CoxB coating layer is further confirmed by atomic resolution HAADF-STEM (Fig. 4g). The uniformity of CoxB coating is conducive to building band coherency between the bulk structure and coating layer as well as surface shielding effects, thus stabilizing the lattice oxygen and mitigating the side reaction of electrode/electrolyte interface to elevate the capability of Li+ storage.

2.3. Conveying the Li+ storage features invoked by structure/interface coupling effect

Since the uniform CoxB coating has been successfully built up, it is of particular interest to investigate its electrochemical properties. The coin-type cells are assembled utilizing the as-designed materials as

a cathode to evaluate their Li+ storage features within a voltage range of 2.0–4.8 V. As shown in Fig. 5a, the initial discharge capacities of the LRM as well as CB-LRM are calculated to be 281.92 and 310.4 mAh g-1, and its Coulombic efficiency (CE) are recorded as 81.8% and 88.0%, respectively, demonstrating that the surface side reaction is considerably mitigated by the structure/interface coupling effect evoked by the coating layer of amorphous CoxB. Moreover, surface oxygen evolution is further studied by in situ differential electrochemical mass spectrometry (Fig. 5b, c) and cyclic voltammetry (CV) (Fig. 5d, g) results. Clearly, oxygen release in the form of CO2 has been effectively mitigated by amorphous CoxB coating, benefitting from the interface bonding and shield effects. Note that the reduced energy barrier for the charge transfer (Fig. 5f, i) and the strengthened electrode/electrolyte interface eventually can facilitate the interfacial transportation process and improve rate capabilities (Fig. S5). Accordingly, the kinetic of Li+ diffusion for the as-designed materials is systematically studied through galvanostatic intermittent titration technique (GITT). As shown in Fig. S6a-f, one selected region at the charging process (~ 4.4 V) is utilized to evaluate the polarization electrochemical process and diffusion capability of Li+. The smaller ΔEt and iR are clearly presented, suggesting that the Li+ diffusion for CB-LRM is efficiently improved, in great line with the electrochemical impedance spectroscopy (EIS) and CV results (Fig. S7 and Fig. 5e, h). Furthermore, to further evaluate their practical application in LIBs, cycling performance of the as-designed materials at different current densities are collected to study the effect of coating layer of amorphous CoxB (Figs. 5j-l and S8). As expected, the discharging specific capacity of CB-LRM could be retained at 218.9 mAh g-1 after 100 loops at 2 C, much higher than that of LRM (189.7 mAh g-1) (Fig. 5l). It is anticipated that, as presented in Fig. 5j, the average voltage decay of discharge process for CB-LRM is only 0.26 V (2.6 mV per cycle) after 100 loops at 1 C. By contrast, the average attenuation of discharging potential for LRM is about 0.317 V (3.17 mV per cycle). Owing to the slower capacity declining and lower voltage degradation (Fig. S9), more than 78.92% energy retention can be retained after 100 cycles for CB-LRM, in contrast, a low energy retention of 72.11% is presented for LRM (Fig. S8b). Such an outstanding cycling stability for CB-LRM should be ascribed to the mitigated lattice oxygen loss, improved stabilities of crystal structure and electrode/electrolyte interface. Based on the discussion above, it is summarized that the superior capabilities of Li+ storage for CB-LRM are successfully realized. Evidently, the excellent electrochemical properties are closely related to the structure/interface coupling effect invoked by the coating layer of amorphous CoxB.

2.4. Unscrambling the electrode/electrolyte interface evolution

As confirmed by the electrochemical performances above, the structure/interface coupling effect induced by the coating layer of amorphous CoxB is conducive to driving the reversible lattice oxygen redox, rending the improved reversibility of Li+ storage. It is well known that, the electrode/electrolyte interface traits are also paramount to the electrochemical performances [22]. It is well documented that intergranular cracking between connected primary particles in a secondary sphere is a critical issue for the degradation of cathodes, especially with higher cut-off voltages and prolonged cycling, mainly leading to the loss of electrical contacts between primary particles, blocking the charge carrier transportation, and finally deteriorating the capability of Li+ storage [23,24]. Moreover, the intergranular cracking is mostly related to mechanical stress produced by anisotropic lattice expansion/shrinkage and heterogeneous charge/discharge kinetics during the electrochemical cycle. To further verify the advantages of structure/interface coupling effect and systematically probe the electrode/electrolyte interface traits, FE-SEM images of the cycled electrodes are utilized to observe morphology intergraty of as prepared CB-LRM and LRM cathodes. As shown in Fig. 6a, b, the broken secondary spheres are obviously observed in LRM electrode due to the anisotropic volume changes associated with the irreversible structure rearrangements and intergranular stress corrosion cracking, which should mainly account for the capacity/voltage decline. In addition, numerous microcracks distributed over the microsphere are found for the LRM electrode after the prolonged cycling, which are usually generated along the grain boundaries from the core and propagated to the surface resulted from the inner anisotropic strain and HF corrosion (Fig. 6a, b). These microcracks undermine the mechanical integrity of the cathode and induce the electrolyte penetration into the particle core, which would exacerbate the surface degradation of the internal primary particles. In contrast, well-preserved rectangular-like morphology and mechanically intact without clear cracks are presented for CB-LRM electrode (Fig. 6d, e), owing to the advantages of structure/interface coupling effect aroused by the coating layer of amorphous CoxB. Furthermore, the HAADF-STEM images of the cycled electrode (Fig. S10) demonstrated that the full encapsulation with the activated interface bonding and shield effect is conducive to mitigating the irreversible phase transformation, therefore enhancing the stability of crystal structure and boosting the Li+ storage capability. Note that, complete elimination of the cracking is still challenging if ever possible, nevertheless, a satisfactory cycling performances over hundreds of cycles may be achieved. The potential mechanism of the robust electrode/electrolyte interface induced by the introduction of coating layer would be further discussed as follow, in details.

It should be pointed out that, the decomposition of electrolyte is considerably aggravated when oxygen radicals are formed in the electrolyte (e.g., hydroxyl HO•, superoxide O2• or O2), which could oxidize the carbonate-solvent under high voltage [22,25,26]. As expected, the curbed oxygen-radicals from the CB-LRM cathode in the electrolyte would greatly mitigate the cathode electrolyte interface over-growth. To further explore the evolution of electrode/electrolyte interface induced by the coating layer of amorphous CoxB, XPS is firstly employed to examine the chemical bonding environment of the cathode surface, with the spectra from C 1s, B 1s, Co 2p and Mn 2p shown in Fig. S11, in which the signals of C 1s (contributed by organic cathode electrolyte interface components, such as polycarbonates and semicarbonates), Co/Mn 2p signals (contributed by Co/Mn-containing cathode electrolyte interface components, such as Co/MnF2) are observed in cycled pristine LRM and CB-LRM. And, it is found that the intensities of XPS spectra for LRM are stronger than that of CB-LRM. Meanwhile, strong Co 2p and B 1s signals are observed in cycled CB-LRM (Fig. S11a, d), indicating that the coating layer of CoxB is not fully covered by thick cathode electrolyte interface, even after the prolonged cycling. Furthermore, the electrode/electrolyte interface of the cycled electrode are also investigated by the TEM, as shown in Fig. S12, the thin cathode electrolyte interface of CB-LRM after 200 cycles at 2 C demonstrated that the amorphous CoxB coating is conducive to reducing the thickness of cathode electrolyte interface, which are mainly resulted from the mitigated the lattice oxygen loss accompanied with the electrolyte decomposition. All the phenomena above suggest a suppressed cathode electrolyte interface over-growth in CB-LRM, mainly resulted from the structure/interface coupling effect induced by the coating layer of amorphous CoxB. Moreover, it should be awared that, the limited probing depth of X-rays used in XPS only captures the chemical bonding environment on the surface and does not provide any information on the layer thickness. Note that, Time of flight secondary ion mass spectrometry (TOF-SIMS) is a powerful tool for investigating the chemical composition, layer thickness, and depth distribution of the decomposition species in the cathode electrolyte interface layer. Therefore, the TOF-SIMS is further applied to investigate the electrode surface after 200 loops at 2 C and conducted the three dimensions (3D) surface reconstruction. Clearly, LRM electrodes are dramatically collapsed as its surface became very rough with much cavity (Fig. 6g-j), in contrast, CB-LRM particles remained well integrated and smooth (Fig. 6k-n), in good line with SEM images in Fig. 6a-f, adequately demonstrating that the construction of coating layer of CoxB is beneficial for enhancing the stability of crystal structure and electrode/electrolyte interface. Usually, the C2H- (Fig. S13b, h) and C2HO- (Fig. S13f, l) fragments are employed to denote the cathode electrolyte interface component in the 3D reconstruction. It is worth noting that, much thinner cathode electrolyte interface layer adhering on the cycled CB-LRM cathode

than on the cycled LRM electrode demonstrate that it obviously remained stable in the CB-LRM cycling, nevertheless, while the carbonate-solvent is seriously destroyed in the LRM cycling. In addition, the PO2- (Fig. S13d, j) and PO3- (Fig. S13e, k) are mainly related to the decomposition of electrolyte. Notably, a relatively weak of PO2- (Fig. S13j) and PO3- (Fig. S13k) signals for the CB-LRM electrode is noticed indicating that the electrolyte decomposition at the CB-LRM cathode is considerably suppressed, in good line with the FE-SEM images (Fig. 6a-e). As shown in Fig. 7a-d and Fig. S13, 3D visualizations are well matched with the abovementioned spectral results (Fig. 7e, f). Moreover, CB-LRM cathode surface also prevented acidic corrosion from the side-products (e.g., HF) in the electrolyte, as the PF6- (Fig. S13i), and MnF3- (Fig. S13g) layers at the CB-LRM cathode surface are much thinner than those at LRM cathode surface (Fig. S13a, c) after 200 loops. The lattice oxygen loss and dissolved TMs in the electrolyte are beneficial to facilitate the thermodynamic and kinetic advantage to the initiation and propagation of stress-corrosion cracking and degrade the cathodes. Evidently, TMs dissolution could be considerably suppressed by mitigating the electrolyte decomposition through the construction of coating layer of amorphous CoxB. Furthermore, considerably uniform LiF2- in the CB-LRM is observed, indicating that the cathode electrolyte interface derived from the CB-LRM should be consisted of more LiF-like inorganic components (which are known to be 'well' cathode electrolyte interface components). Note that the overall structure of the cathode electrolyte interface in both LRM and CB-LRM cathodes displays a double-layer (as indicated by the yellow and blue areas in Fig. 7e, f): the outer layer primarily consists of metal-related species (LiF2, MnF3-, etc.,), while the inner layer is dominated by the electrolyte decomposition-bearing fragments. Besides, the cathode electrolyte interface species in LRM extend to a longer depth on the surface than in CB-LRM, implying the formation of a thicker cathode electrolyte interface on LRM after cycling. Taken together, much-thinner and robust cathode electrolyte interface layer at the CB-LRM cathode surface, presenting less fluoride, would be conducive to faster Li+ transfer, mitigating the TMs dissolution and safeguarding the TMs redox couples, verified by the EIS (Fig. S7) and GITT results (Fig. S6). In brief, these intrigued phenomena considerably confirmed that the coating layer of amorphous CoxB for the CB-LRM is conducive to dramatically mitigating the electrolyte decomposition and subsequent TMs dissolution, resulting in a ruggedized electrode/electrolyte interface and structure/thermal stability. Based on the results above, it is concluded that the construction of coating layer of amorphous CoxB would arouse the structure/interface coupling effect, which are beneficial for driving the reversible lattice oxygen redox induced by the excited interface-reconstruction and boosting the stability of electrode/electrolyte interface resulted from the alleviated cauterization of electrolyte invoked by the electrolyte decomposition. Furthermore, it is proposed that engineering the functionalized coating layer with interface bonding effect would be a potential route to optimize

the electrochemical performances of Li-rich Mn-based oxide cathodes or the congeneric electrode materials. The suggested structure/interface coupling effect and its mitigation offer new insights into the intertwined electro-chemo-mechanics of oxide cathodes under fickle electrochemical environments and consistent with recent advance in optimizing bulk electrode composition and crystallography.

3. Conclusions

In summary, CB-LRM with integrally encapsulated by amorphous CoxB is successfully designed via an autocatalytic plating strategy. Interestingly, band coherency is ingeniously invoked by the interface-reconstruction between bulk structure and amorphous coating layer, which would lower the energy of O 2p states associated with the strengthened orbital hybridization of O 2p-Mn 3d to increase the formation energy of oxygen vacancies, therefore considerably mitigating the lattice oxygen loss. Meanwhile, interface shielding effect is aroused by the integrally coating layer of amorphous CoxB, which is conducive to protecting the electrode against the electrolyte corrosion along with subsequent TMs dissolution, and ultimately rendering a well-knit electrode/electrolyte interface. Greatly, the as-designed CB-LRM renders excellent long cycling stability after 100 loops with only 0.154% capacity fading and 2.60 mV potential decline per cycle. Meaningfully, such strategy is anticipated to offer reference for rationally designing the congeneric energy-storage materials.

Declaration of Competing Interest

The authors declare that they have no known competing financial interests or personal relationships that could have appeared to influence the work reported in this paper.

Acknowledgments

This work was financially supported by National Natural Science Foundation of China (U20A20247), National Key Research and Development Program of China (2019YFC1907805) and Fundamental Research Funds for the Central Universities of Central South University (2021zzts0072). A.D, T.L and K.A acknowledge support from the US Department of Energy (DOE), Office of Energy Efficiency and Renewable Energy (EERE), Vehicle Technologies Office (VTO). This work was also supported by Clean Vehicles, US-China Clean Energy Research centre (CERC-CVC2) under the US DOE EERE Vehicle Technologies Office. This research used resources of the Center for Nanoscale Materials including transmission electron microscopy, U.S. Department of Energy (DOE) Office of Science User Facilities operated for the DOE Office of Science and Office of Basic Energy Sciences. Argonne National Laboratory is operated for the DOE Office of Science by the UChicago Argonne, LLC, under contract no. DE-AC02-06CH11357. J.C. thanks the Shiyanjia Lab (www.shiyanjia.com) for the STEM and XPS characterization as well as Chunlin Tan (Wechat: EditorTan) for his help with the image illustrations.

References

[1] J. Liu, J. Wang, Y. Ni, K. Zhang, F. Cheng, J. Chen; Recent breakthroughs and perspectives of high-energy layered oxide cathode materials for lithium ion batteries; Mater. Today, 43 (2021), pp. 132-165

[2] H. Hasnain, S. Kosuke, B. Bernardo, T. Naruki, Y. Naoaki, Y. Kentaro, O. Yuki, U. Yoshiharu, S. Yoshiharu, S. Hiroshi, B. Arun, V. Venkatasubramanian; Tomographic reconstruction of oxygen orbitals in lithium-rich battery materials; Nature, 594 (2021), pp. 213-216

[3] P.M. Csernica, S.S. Kalirai, W.E. Gent, K. Lim, Y.-.S. Yu, Y. Liu, S.-.J. Ahn, E. Kaeli, X. Xu, K.H. Stone, A.F. Marshall, R. Sinclair, D.A. Shapiro, M.F. Toney, W.C. Chueh; Persistent and partially mobile oxygen vacancies in Li-rich layered oxides; Nat. Energy, 6 (2021), pp. 642-652

[4] R.A. House, J.-.J. Marie, M.A. Pérez-Osorio, G.J. Rees, E. Boivin, P.G. Bruce; The role of O2 in O-redox cathodes for Li-ion batteries; Nat. Energy, 6 (2021), pp. 781-789

[5] S. Yin, W. Deng, J. Chen, X. Gao, G. Zou, H. Hou, X. Ji; Fundamental and solutions of microcrack in Ni-rich layered oxide cathode materials of lithium-ion batteries; Nano Energy, 83 (2021), Article 105854

[6] W. He, W. Guo, H. Wu, L. Lin, Q. Liu, X. Han, Q. Xie, P. Liu, H. Zheng, L. Wang, X. Yu, D.-.L. Peng; Challenges and recent advances in high capacity Li-rich cathode materials for high energy density lithium-ion batteries; Adv. Mater., 33 (2021), Article 2005937

[7] H. Hou, C.E. Banks, M. Jing, Y. Zhang, X. Ji; Carbon quantum dots and their derivative 3D porous carbon frameworks for sodium-ion batteries with ultralong cycle life; Adv. Mater., 27 (2015), pp. 7861-7866

[8] T. Liu, J. Liu, L. Li, L. Yu, J. Diao, T. Zhou, S. Li, A. Dai, W. Zhao, S.Y.Ren Xu, L. Wang, T. Wu, R. Qi, Y. Xiao, J. Zheng, W. Cha, R. Harder, I. Robinson, J. Wen, J. Lu, F. Pan, K. Amine; Origin of structural degradation in Li-rich layered oxide cathode; Nature, 606 (2022), pp. 305-312

[9] T. Liu, L. Yu, J. Liu, J. Lu, X. Bi, A. Dai, M. Li, M. Li, Z. Hu, L. Ma, D. Luo, J. Zheng, T. Wu, Y. Ren, J. Wen, F. Pan, K. Amine; Understanding Co roles towards developing Co-free Ni-rich cathodes for rechargeable batteries; Nat. Energy, 6 (2021), pp. 277-286

[10] Q. Wang, S. Mariyappan, G. Rousse, A.V. Morozov, B. Porcheron, R. Dedryvère, J. Wu, W. Yang, L. Zhang, M. Chakir, M. Avdeev, M. Deschamps, Y.-.S. Yu, J. Cabana, M.-.L. Doublet, A.M. Abakumov, J.-.M. Tarascon; Unlocking anionic redox activity in O3-type sodium 3d layered oxides via Li substitution; Nat. Mater., 20 (2021), pp. 353-361

[11] M. Yoon, Y. Dong, J. Hwang, J. Sung, H. Cha, K. Ahn, Y. Huang, S.J. Kang, J. Li, J. Cho; Reactive boride infusion stabilizes Ni-rich cathodes for lithium-ion batteries; Nat. Energy, 6 (2021), pp. 362-371

[12] J. Chen, W. Deng, X. Gao, S. Yin, L. Yang, H. Liu, G. Zou, H. Hou, X. Ji; Demystifying the lattice oxygen redox in layered oxide cathode materials of lithium-ion batteries; ACS Nano, 15 (2021), pp. 6061-6104

[13] X. Yu; Releasing oxygen from the bulk; Nat. Energy, 6 (2021), pp. 572-573

[14] J. Chen, G. Zou, W. Deng, Z. Huang, X. Gao, C. Liu, S. Yin, H. Liu, X. Deng, Y. Tian, J. Li, C. Wang, D. Wang, H. Wu, L. Yang, H. Hou, X. Ji; Pseudo-bonding and electric-field harmony for Li-rich Mn-based oxide cathode; Adv. Funct. Mater., 30 (2020), Article 2004302

[15] J. Deng, X. Yu, X. Qin, D. Zhou, L. Zhang, H. Duan, F. Kang, B. Li, G. Wang; Co—B nanoflakes as multifunctional bridges in ZnCo2O4 micro-/nanospheres for superior lithium storage with boosted kinetics and stability; Adv. Energy Mater., 9 (2019), Article 1803612

[16] J. Masa, P. Weide, D. Peeters, I. Sinev, W. Xia, Z. Sun, C. Somsen, M. Muhler, W. Schuhmann; Amorphous cobalt boride (Co2B) as a highly efficient nonprecious catalyst for electrochemical water splitting: oxygen and hydrogen evolution; Adv. Energy Mater., 6 (2016), Article 1502313

[17] R.A. House, U. Maitra, M.A. Pérez-Osorio, J.G. Lozano, L. Jin, J.W. Somerville, L.C. Duda, A. Nag, A. Walters, K. Zhou, M.R. Roberts, P.G. Bruce; Superstructure control of first-cycle voltage hysteresis in oxygen-redox cathodes; Nature, 577 (2020), pp. 502-508

[18] J. Huang, P. Zhong, Y. Ha, D.-.H. Kwon, M.J. Crafton, Y. Tian, M. Balasubramanian, B.D. McCloskey, W. Yang, G. Ceder; Non-topotactic reactions enable high rate capability in Li-rich cathode materials; Nat. Energy, 6 (2021), pp. 706-714

[19] K. Zhang, Z. Jiang, F. Ning, B. Li, H. Shang, J. Song, Y. Zuo, T. Yang, G. Feng, X. Ai, D. Xia; Metal-ligand π interactions in lithium-rich Li2RhO3 cathode material activate bimodal anionic redox; Adv. Energy Mater., 11 (2021), Article 2100892

[20] B. Li, H. Yan, J. Ma, P. Yu, D. Xia, W. Huang, W. Chu, Z. Wu; Manipulating the electronic structure of Li-rich manganese-based oxide using polyanions: towards better electrochemical performance; Adv. Funct. Mater., 24 (2014), pp. 5112-5118

[21] Y. Bi, J. Tao, Y. Wu, L. Li, Y. Xu, E. Hu, B. Wu, J. Hu, C. Wang, J.-.G. Zhang, Y. Qi, J. Xiao; Reversible planar gliding and microcracking in a single-crystalline Ni-rich cathode; Science, 370 (2020), pp. 1313-1317

[22] J. Zhao, X. Zhang, Y. Liang, Z. Han, S. Liu, W. Chu, H. Yu; Interphase engineering by electrolyte additives for lithium-rich layered oxides: advances and perspectives; ACS Energy Lett, 6 (2021), pp. 2552-2564

[23] S. Lee, W. Li, A. Dolocan, H. Celio, H. Park, J.H. Warner, A. Manthiram; In-depth analysis of the degradation mechanisms of high-nickel, low/no-cobalt layered oxide cathodes for lithium-ion batteries; Adv. Energy Mater., 11 (2021), Article 2100858

[24] Y. Su, Q. Zhang, L. Chen, L. Bao, Y. Lu, S. Chen, F. Wu; Stress accumulation in Ni-rich layered oxide cathodes: origin, impact, and resolution; J. Energy Chem., 65 (2022), pp. 236-253

[25] C.-.C. Su, M. He, J. Shi, R. Amine, Z. Yu, L. Cheng, J. Guo, K. Amine; Principle in developing novel fluorinated sulfone electrolyte for high voltage lithium-ion batteries; Energy Environ. Sci., 14 (2021), pp. 3029-3034

[26] W. Liu, J. Li, W. Li, H. Xu, C. Zhang, X. Qiu; Inhibition of transition metals dissolution in cobalt-free cathode with ultrathin robust interphase in concentrated electrolyte; Nat. Commun., 11 (2020), Article 3629

Fig. 1. Density functional theory calculation of the globally band coherency. (a) Atomic structure of the coating engineering. (b) 2 dimensional slices of the charge density distribution of a simulated interface between the Li2MnO3 (131) surface and amorphous CoxB. Projected density of states and schematic local environment (c-e insets) of lattice oxygen coordinated by two Mn and four Li atoms (c), interface oxygen coordinated by one Co, one Mn and three Li atoms (d) and interface oxygen coordinated by one B, one Mn and three Li atoms (e). (f) Formation energy of oxygen vacancy.

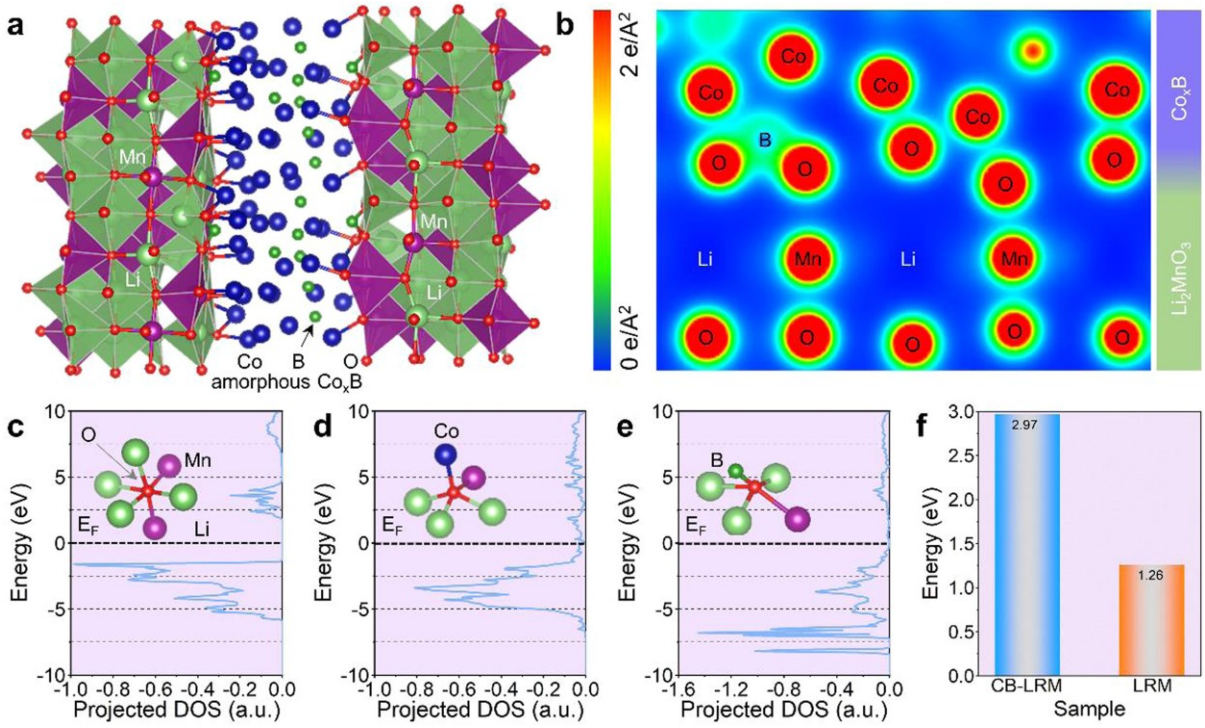

Fig. 2. Schematic illustration of the autocatalytic plating and morphology characterization for the as-designed samples. (a) Schematic illustration of the preparation process of the CB-LRM. The morphology characterization and EDS mapping images for the as-prepared (b-d) pristine LRM and (e-g) CB-LRM, respectively.

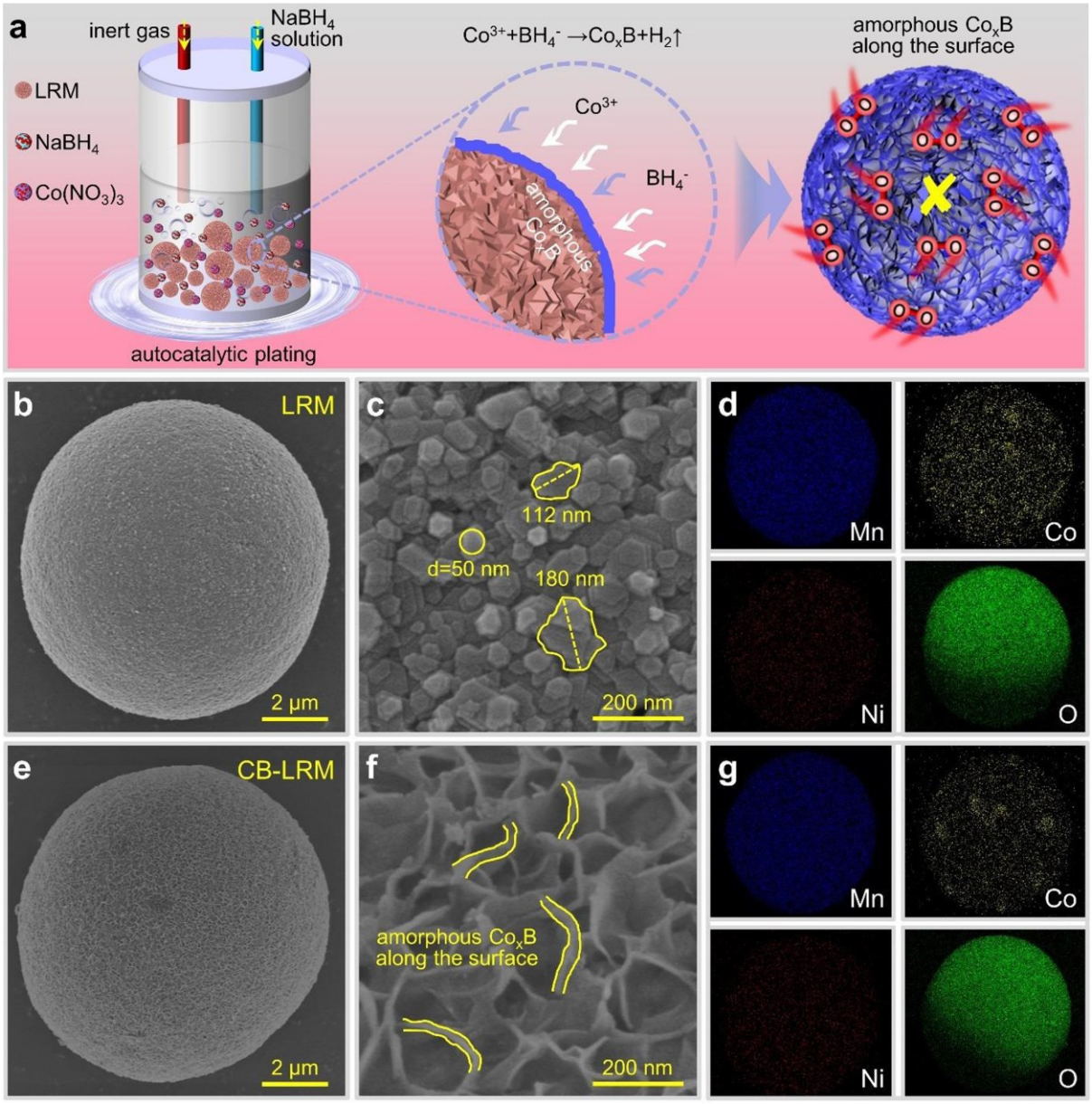

Fig. 3. Demystifying the crystal structure and surface composition of the as-obtained samples. (a, b) Rietveld refinements results of XRD patterns for the as-obtained samples. (c) XRD patterns of the as-prepared CoxB. (d-f) XPS spectra of B 1s, Co 2p and O 1s for the as-designed samples.

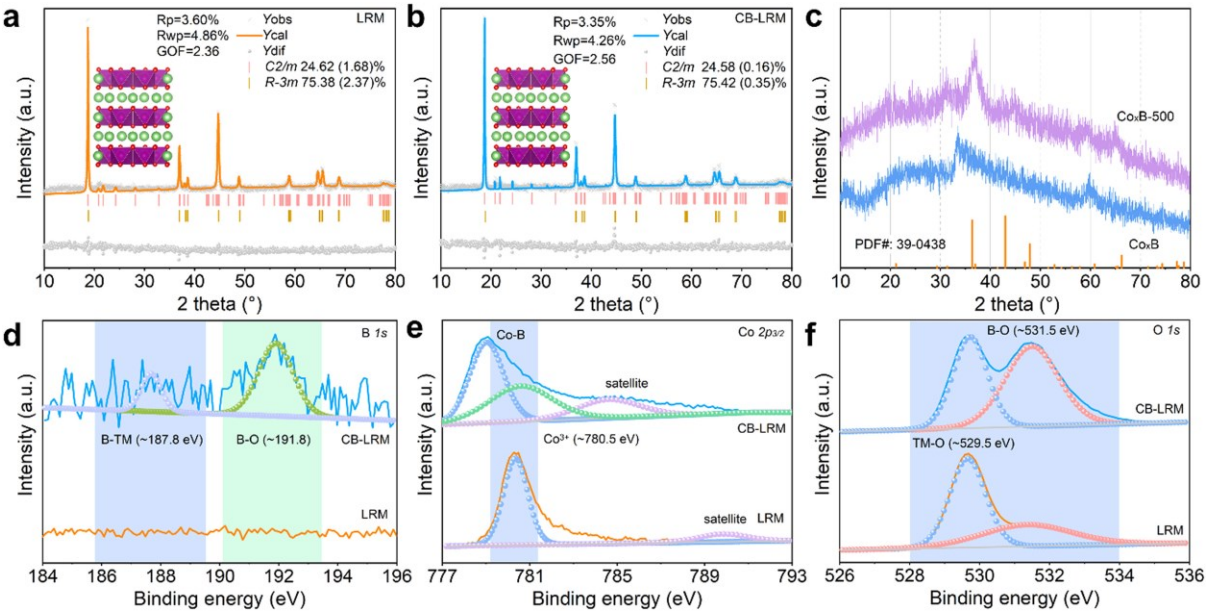

Fig. 4. Structure/interface characterization for the CB-LRM. (a-c) TEM and SAED images. (d-f) ABF/HAADF-STEM images. (g, h) HAADF-STEM and EELS mapping images.

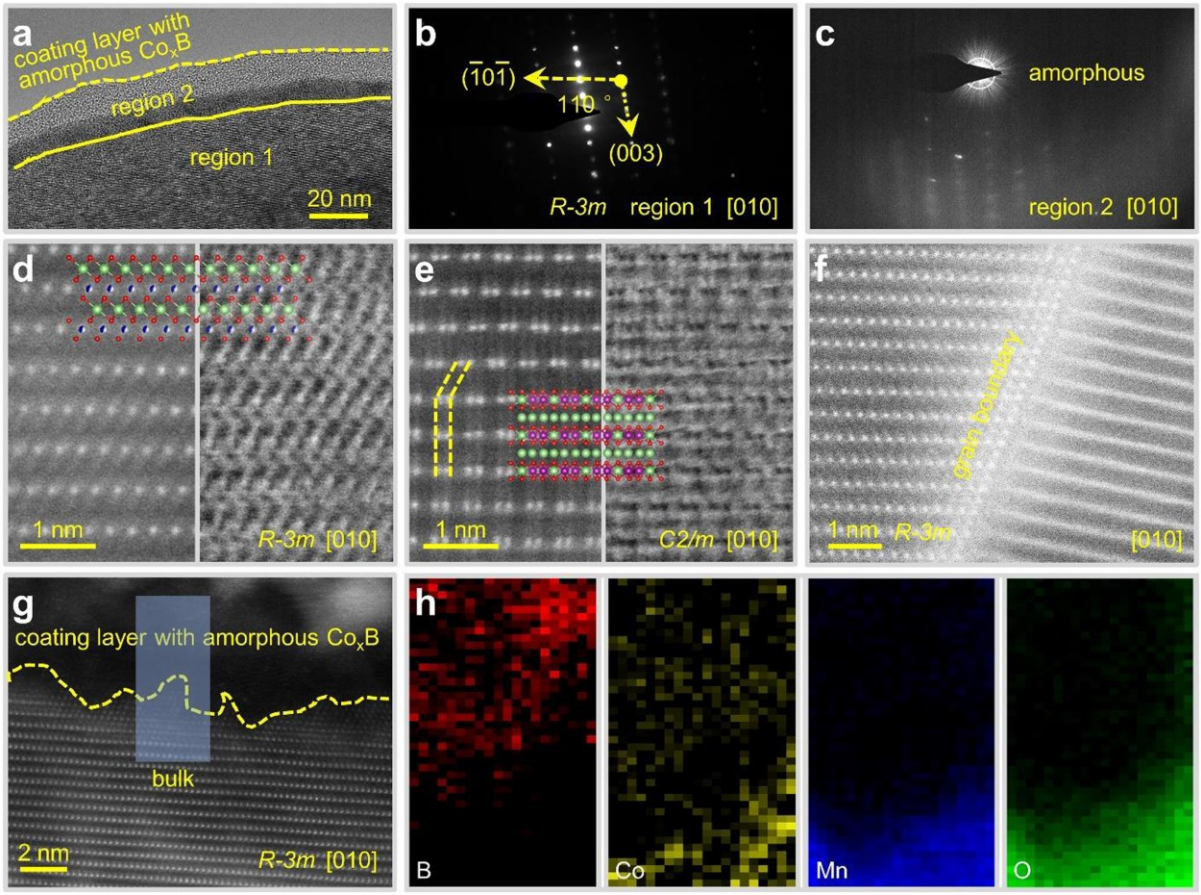

Fig. 5. Conveying the Li+ storage features invoked by the structure/interface coupling effect. (a) Initial charge-discharge curves and the corresponding CE at 0.1 C. (b, c) CO2 (m/z = 44) gas evolution and corresponding voltage profiles. (d, g) CV curves at 0.05 mV/s. (e, h). CV curves at different scan rate. (f, i) Voltage gap and polarization. (j) Average voltage of the as-obtained samples at 1 C. (k, l) Energy density and specific capacity of the as-obtained samples at 2 C, respectively.

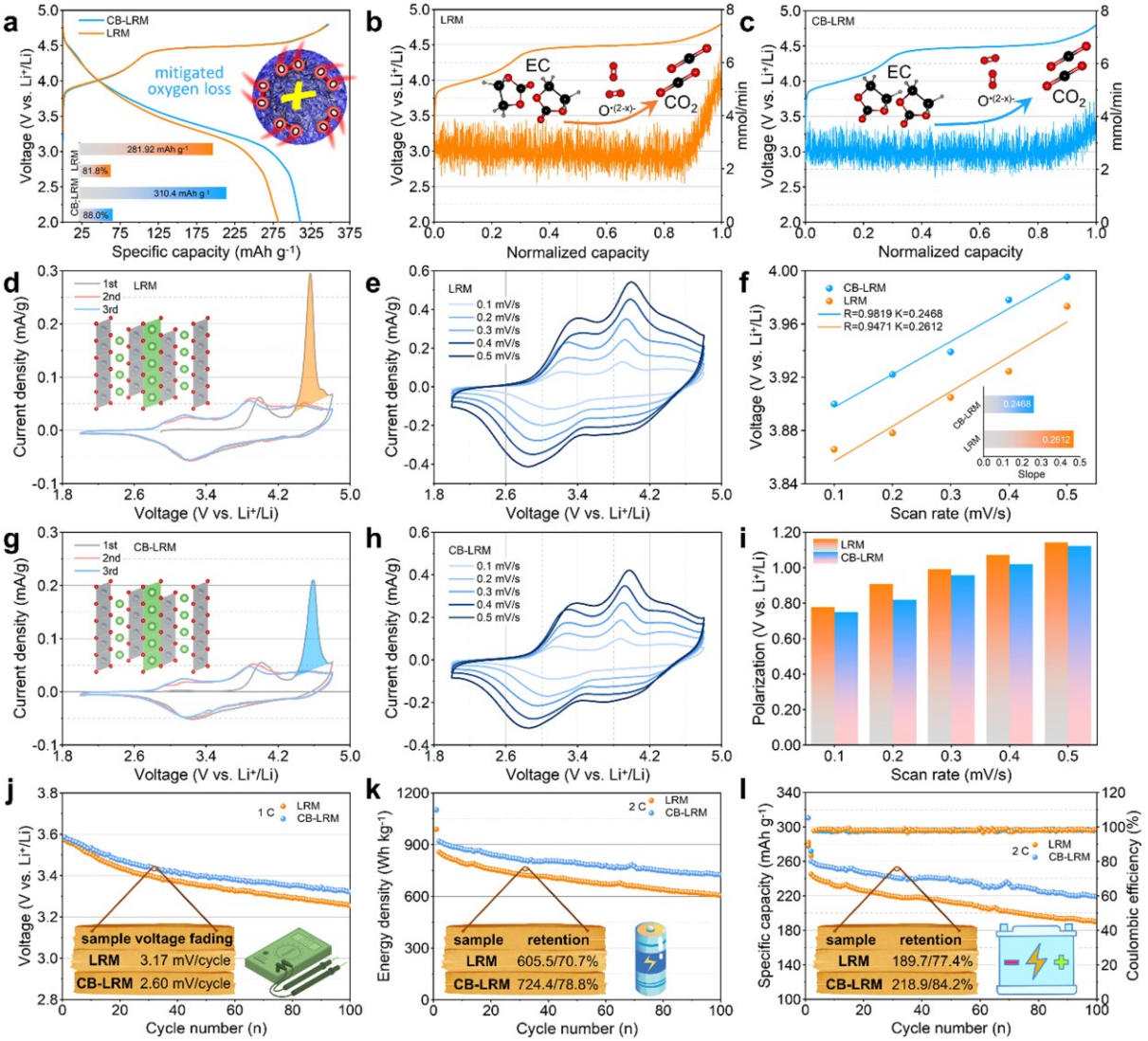

Fig. 6. Morphology and chemical composition evolution after 200 cycles at 2 C. Morphology transformation of (a-c) LRM and (d-f) CB-LRM electrodes. Comparative chemical mapping of various secondary-ion species as a function of sputtering time, demonstrating the complexity, and dynamic evolution of the cathode interphase of (g-j) LRM and (k-n) CB-LRM, respectively. Scale bars, 3 μm (g-n).

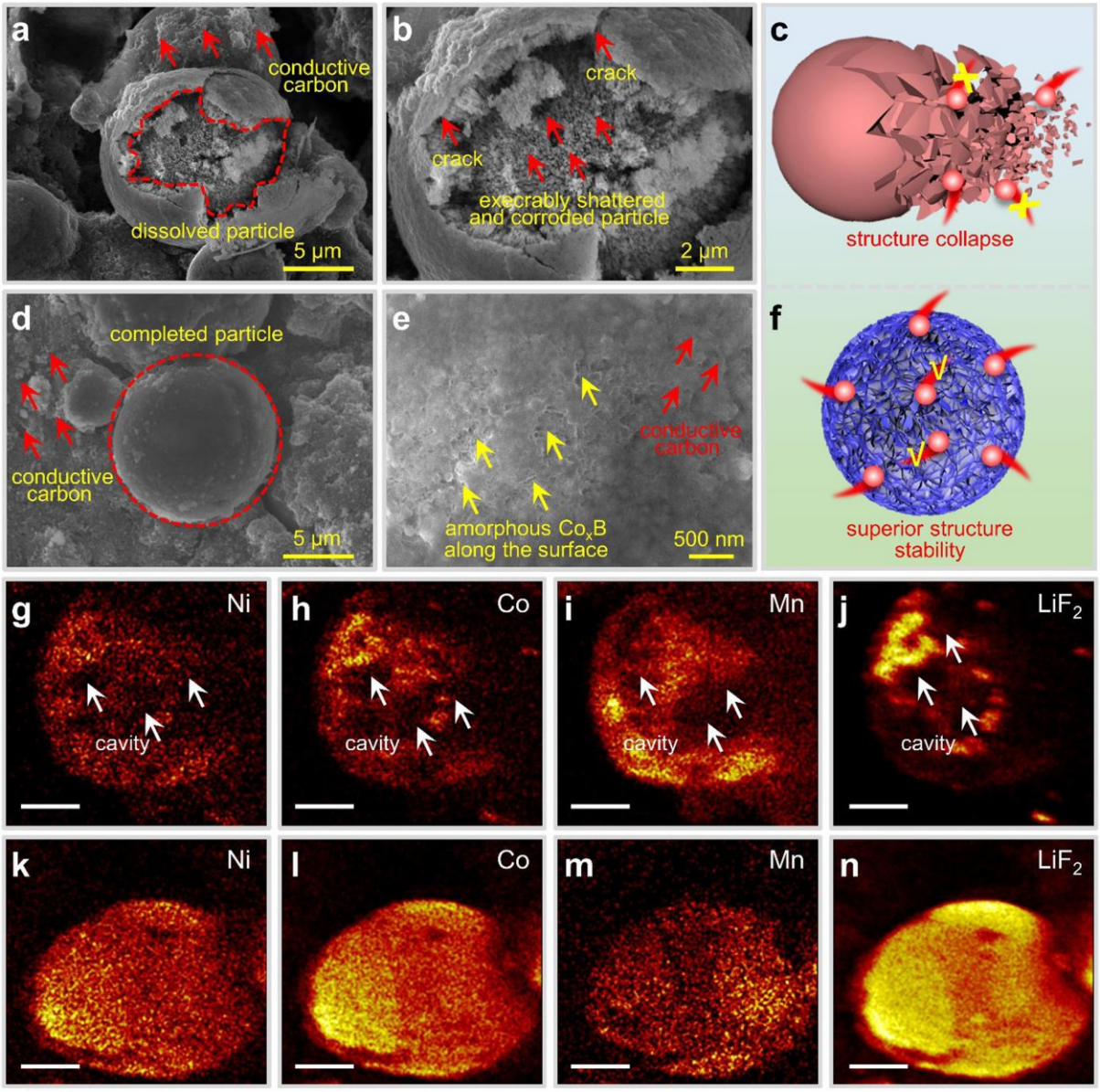

Fig. 7. Dissecting the electrode/electrolyte interface evolution after 200 cycles at 2 C. (a, b) The 3D reconstruction of PO2F2- and LiF2- fragment for the LRM electrodes. (c, d) The 3D reconstruction of PO2F2- and LiF2- fragment for the CB-LRM electrodes. (e, f) TOF-SIMS normalized depth profiles of diverse kinds of secondary-ion fragments constituting the cathode electrolyte interface of LRM and CB-LRM, respectively.